Supplementary material for 'Nonuniversality and Dissipative Anomaly in Compressible Magnetohydrodynamic Turbulence'

C. Li,[1,2] Y. Yang,[3] W.H. Matthaeus,[3] B. Jiang,[1,2] M. Wan,[1,2,*] and S. Chen[4,1,2]

[1]*Guangdong Provincial Key Laboratory of Turbulence Research and Applications, Department of Mechanics and Aerospace Engineering, Southern University of Science and Technology, Shenzhen 518055, China*

[2]*Guangdong-Hong Kong-Macao Joint Laboratory for Data-Driven Fluid Mechanics and Engineering Applications, Southern University of Science and Technology, Shenzhen 518055, China*

[3]*Department of Physics and Astronomy, University of Delaware, DE 19716, USA*

[4]*Eastern Institute for Advanced Study, Eastern Institute of Technology, Ningbo 315200, China*

SIMULATION DETAILS

The details of all simulation cases are summarized in Table I and II. Here N denotes the simulation resolution, and R_L^- the generalized Reynolds number defined in (6). The Taylor-scale Reynolds number R_λ and the turbulent Mach number M_t are defined as

$$R_\lambda = \mathrm{Re}\frac{\langle\rho\rangle\, u'\lambda}{\langle\mu\rangle}\,, \quad M_t = \mathrm{M}\frac{\sqrt{3}u'}{\left\langle T^{1/2}\right\rangle}\,. \tag{1}$$

$\delta_c = u'_c/u'$ denotes the compressibility parameter, and $k_{\max} = N/2$ the largest resolved wave number in simulations. The kinetic and magnetic Kolmogorov length-scales are defined as

$$\eta_u = \mathrm{Re}^{-3/4}\left(\langle\nu\rangle^3/\varepsilon_k\right)^{1/4}\,, \quad \eta_m = \mathrm{Re}_\mathrm{m}^{-3/4}\left(\langle\nu\rangle^3/\varepsilon_m\right)^{1/4}\,. \tag{2}$$

L_u denotes the kinetic integral length, $\theta_\mathrm{rms}\,, \omega_\mathrm{rms}$ and j_rms the rms values of dilatation field $\theta = \boldsymbol{\nabla}\cdot\boldsymbol{u}$, vorticity field $\boldsymbol{\omega} = \boldsymbol{\nabla}\times\boldsymbol{u}$ and magnetic current density $\boldsymbol{j} = \boldsymbol{\nabla}\times\boldsymbol{b}$, respectively. The parameter $\rho_c = 2\langle\boldsymbol{u}\cdot\boldsymbol{b}\rangle/\left\langle\boldsymbol{u}^2+\boldsymbol{b}^2\right\rangle$ denotes the normalized cross helicity, while $H_m = \langle\boldsymbol{a}\cdot\boldsymbol{b}\rangle$ the magnetic helicity.

TABLE I: Specifications of all simulation cases (Series A, B, C & D).

Case	N	R_L^-	R_λ	M_t	δ_c	$k_{\max}\eta_u$	$k_{\max}\eta_m$	L_u/η_u	$\theta_{\rm rms}$	$\omega_{\rm rms}$	$j_{\rm rms}$	ρ_c	H_m
A1	256	104.2	49.8	0.20	0.36	8.25	9.27	28	1.6	4.5	3.8	0.02	0.012
A2	256	207.3	80.7	0.20	0.39	5.27	4.97	43	2.0	5.5	6.7	0.04	-0.014
A3	256	303.5	105.4	0.21	0.39	3.93	3.63	56	2.4	6.6	8.3	0.00	-0.002
A4	256	400.2	122.0	0.21	0.40	3.14	2.76	70	2.8	7.7	10.8	-0.01	-0.003
A5	256	488.7	144.4	0.21	0.38	2.71	2.37	80	3.0	8.3	11.7	0.04	-0.004
A6	256	602.0	156.2	0.21	0.41	2.37	2.03	92	3.1	9.1	13.4	-0.02	-0.002
A7	384	889.8	197.9	0.21	0.39	2.65	2.24	122	3.7	10.9	16.5	-0.02	-0.005
A8	512	1526.5	251.6	0.21	0.41	2.25	1.90	191	4.7	15.3	22.9	-0.03	-0.002
B1	256	103.9	32.7	0.20	0.61	7.79	10.79	30	3.5	3.8	2.9	0.04	0.003
B2	256	206.3	58.2	0.21	0.61	4.98	6.07	45	4.0	4.9	4.5	0.00	0.002
B3	256	406.6	99.4	0.21	0.62	3.24	3.28	69	4.7	5.8	7.8	-0.01	0.005
B4	256	504.5	115.3	0.21	0.62	2.73	2.60	82	5.1	6.7	9.9	-0.01	-0.007
B5	256	607.3	140.9	0.21	0.63	2.51	2.43	88	4.9	6.8	9.4	0.01	-0.001
B6	256	789.2	170.4	0.21	0.63	2.03	1.88	108	5.3	8.0	11.7	0.02	0.004
B7	384	1114.7	203.3	0.21	0.61	2.45	2.24	136	6.0	9.0	13.6	-0.02	0.006
B8	512	1592.1	230.3	0.21	0.65	2.34	2.14	186	7.7	12.3	18.2	0.00	0.017
C1	256	105.6	23.0	0.20	0.84	7.01	15.39	33	5.6	2.2	1.4	0.00	0.001
C2	256	210.2	42.4	0.21	0.83	4.59	8.09	50	6.5	2.7	2.6	0.00	0.002
C3	256	408.1	76.8	0.21	0.85	3.05	4.35	74	7.2	3.4	4.5	0.03	-0.004
C4	256	513.3	96.4	0.21	0.85	2.69	3.72	84	7.4	3.5	4.9	0.02	-0.001
C5	256	618.1	111.6	0.21	0.85	2.43	3.18	93	7.5	3.9	5.6	0.02	-0.001
C6	256	846.8	146.2	0.21	0.85	2.07	2.54	109	7.6	4.4	6.6	-0.03	0.009
C7	384	1115.3	190.4	0.22	0.80	2.39	2.91	141	9.2	5.4	8.3	0.01	0.006
C8	512	1546.9	267.5	0.24	0.76	2.45	2.92	182	10.7	6.7	10.0	0.07	-0.008
D1	256	105.0	50.1	0.61	0.34	8.27	10.49	28	1.6	4.5	3.2	0.03	-0.004
D2	256	202.5	81.8	0.63	0.33	5.17	5.43	43	2.3	5.7	5.9	0.02	0.003
D3	256	303.8	110.2	0.63	0.33	3.97	3.86	56	2.5	6.5	7.7	0.05	0.004
D4	256	406.5	131.3	0.63	0.33	3.24	2.90	68	2.7	7.4	10.2	0.00	0.009
D5	256	600.4	170.4	0.63	0.33	2.45	2.17	89	3.0	8.7	12.2	0.03	0.002
D6	256	800.3	205.8	0.63	0.34	2.03	1.75	109	2.9	9.7	14.0	-0.02	-0.011
D7	384	1163.5	242.0	0.64	0.34	2.15	1.84	149	3.5	13.0	19.0	0.05	0.008
D8	512	1721.1	297.1	0.64	0.33	2.11	1.81	202	4.1	16.2	23.4	0.03	0.004
D9	768	2851.4	386.1	0.64	0.34	2.16	1.85	296	4.8	20.9	30.1	-0.02	-0.002

TABLE II: Specifications of all simulation cases (Series E, F, P & Q).

Case	N	R_L^-	R_λ	M_t	δ_c	$k_{\max}\eta_u$	$k_{\max}\eta_m$	L_u/η_u	$\theta_{\rm rms}$	$\omega_{\rm rms}$	$j_{\rm rms}$	ρ_c	H_m
E1	256	110.7	36.1	0.64	0.58	7.73	12.44	30	3.8	3.9	2.5	-0.02	0.002
E2	256	212.1	59.1	0.64	0.60	4.97	6.02	45	4.6	4.8	5.3	0.03	0.000
E3	256	323.7	82.8	0.65	0.59	3.82	4.25	58	5.0	5.6	7.1	-0.02	-0.002
E4	256	419.8	102.6	0.65	0.61	3.19	3.32	69	5.3	6.3	8.8	0.01	-0.003
E5	256	647.4	137.7	0.65	0.63	2.44	2.35	91	5.6	7.6	11.6	0.01	-0.008
E6	256	796.4	174.1	0.65	0.59	2.13	2.05	103	5.5	8.0	11.8	0.00	0.006
E7	384	1041.5	203.5	0.66	0.59	2.61	2.47	126	6.4	9.2	14.2	-0.02	0.001
E8	512	1561.2	287.1	0.68	0.55	2.41	2.24	180	7.4	12.7	19.0	0.07	-0.001
E9	768	2959.2	375.3	0.65	0.60	2.30	2.11	281	9.3	17.3	26.1	0.03	0.001
F1	256	113.3	30.8	0.69	0.70	7.10	14.97	32	5.4	3.4	1.9	0.00	0.000
F2	256	227.0	48.0	0.67	0.73	4.56	6.22	49	6.4	4.3	5.4	-0.01	-0.003
F3	256	331.0	67.3	0.66	0.72	3.61	4.90	62	6.8	4.7	5.8	0.02	0.002
F4	256	439.4	91.6	0.68	0.73	3.07	3.86	72	6.9	5.3	7.1	0.01	0.000
F5	256	652.8	128.1	0.66	0.74	2.46	2.87	90	6.8	6.0	8.4	0.00	0.001
F6	256	865.6	160.1	0.66	0.73	2.02	2.17	109	7.2	7.0	10.8	0.02	-0.001
F7	384	1198.7	188.4	0.67	0.73	2.38	2.53	139	8.6	8.5	13.4	-0.02	-0.004
F8	512	1705.2	250.1	0.68	0.73	2.48	2.55	177	9.5	10.1	16.2	0.02	0.001
P1	256	218.7	40.8	0.43	0.81	4.49	6.93	50	6.9	3.3	3.9	-0.02	-0.002
P2	256	323.0	55.4	0.42	0.82	3.53	4.87	64	7.3	3.8	5.3	0.00	0.002
P3	256	435.0	75.3	0.42	0.82	3.06	4.10	73	7.2	4.3	5.6	-0.03	0.000
P4	256	640.1	113.6	0.42	0.81	2.46	3.01	91	7.2	4.9	6.8	0.00	0.001
P5	256	861.0	145.3	0.42	0.82	2.07	2.35	108	7.4	5.6	8.4	-0.03	0.001
P6	384	1253.3	183.3	0.43	0.80	2.27	2.54	147	9.1	7.1	11.0	0.01	0.018
P7	512	2047.8	267.7	0.44	0.80	2.14	2.27	205	10.4	9.5	14.7	0.02	0.001
P8	768	3205.8	357.2	0.45	0.80	2.25	2.36	290	12.8	12.8	19.4	0.03	-0.002
Q1	256	218.3	42.5	0.47	0.85	4.28	10.89	53	8.0	2.2	1.7	0.01	-0.001
Q2	256	328.8	50.6	0.44	0.94	3.38	7.65	66	8.6	2.6	2.3	0.00	0.005
Q3	256	435.7	76.1	0.47	0.87	2.91	6.17	76	8.6	3.2	2.6	0.00	0.000
Q4	256	594.0	86.0	0.43	0.96	2.49	4.80	90	8.7	2.7	3.2	0.00	-0.004
Q5	256	766.8	127.4	0.46	0.90	2.17	3.70	103	8.8	3.3	4.0	0.00	0.001
Q6	384	1303.8	161.2	0.44	0.94	2.25	3.75	148	10.8	4.1	5.4	0.00	0.004
Q7	512	2129.3	235.8	0.44	0.92	2.11	2.92	206	12.5	6.6	9.3	0.01	0.002

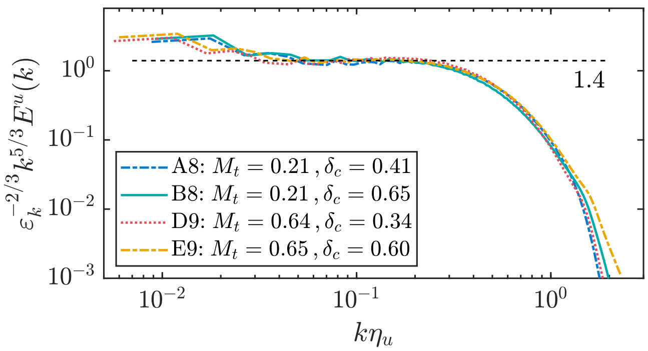

(a) Compensated kinetic spectrum of cases with low $\delta_c = u_c'/u'$.

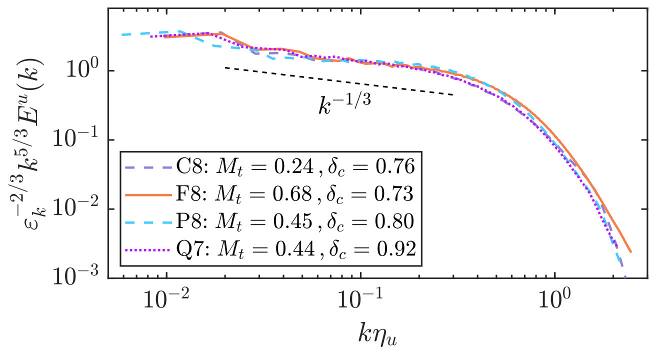

(b) Compensated kinetic spectrum of cases with high $\delta_c = u_c'/u'$.

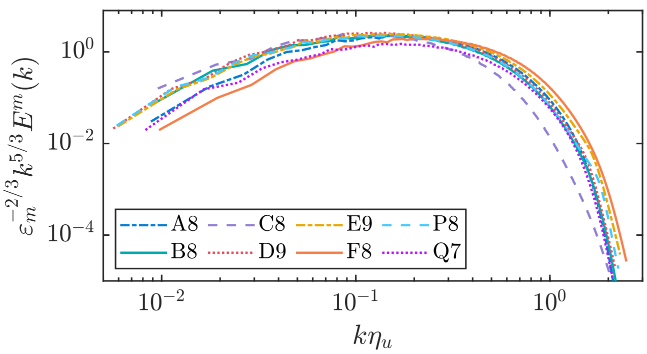

(c) Compensated magnetic spectrum

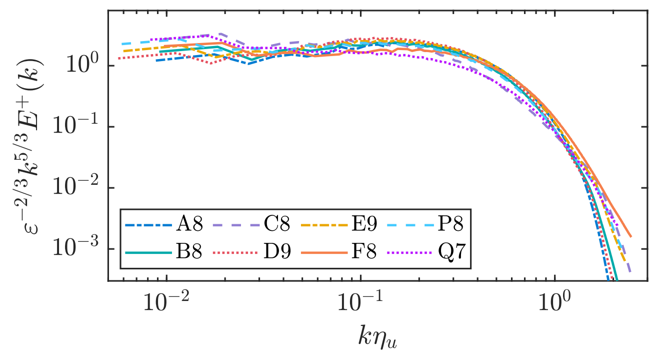

(d) Compensated Elsässer spectrum

FIG. 1: Compensated spectrum of selective DNS cases.

THE SPECTRUM OF SELECTIVE SIMULATION CASES

The compensated kinetic spectrum $\varepsilon_k^{-2/3} k^{5/3} E^u(k)$, magnetic spectrum $\varepsilon_m^{-2/3} k^{5/3} E^m(k)$ and Elsässer spectrum $\varepsilon^{-2/3} k^{5/3} E^+(k)$ of selected simulation cases are plotted in Fig. 1. Here $\varepsilon_k\,, \varepsilon_m$ are the kinetic and magnetic dissipation rate (per unit mass):

$$\varepsilon_k = \mathrm{Re}^{-1} \left\langle \sigma_{ij} S_{ij} / \rho \right\rangle \,, \quad \varepsilon_m = \mathrm{Re}_\mathrm{m}^{-1} \left\langle \eta \boldsymbol{j}^2 / \rho \right\rangle \,, \tag{3}$$

and $\varepsilon = \varepsilon_k + \varepsilon_m$ denotes the total dissipation. $E^u(k)\,, E^m(k)\,, E^+(k)$ denote the spectrum of velocity field $\boldsymbol{u}$, magnetic field $\boldsymbol{b}$, and Elsässer variable $\boldsymbol{z}_+ = \boldsymbol{u} + \boldsymbol{b}/\sqrt{\rho}$ respectively, and satisfy

$$\int_0^\infty E^u(k)\, \mathrm{d}k = \frac{1}{2} \left\langle \boldsymbol{u}^2 \right\rangle \,, \quad \int_0^\infty E^m(k)\, \mathrm{d}k = \frac{1}{2} \left\langle \boldsymbol{b}^2 \right\rangle \,, \quad \int_0^\infty E^+(k)\, \mathrm{d}k = \frac{1}{2} \left\langle \boldsymbol{z}_+^2 \right\rangle \,. \tag{4}$$

For cases with low to moderate compressibility (see Fig. 1(a)), the solenoidal field dominates and thus kinetic spectrum fits well with the classical $k^{-5/3}$ power law, with the Kolmogorov constant $C_K \approx 1.4$. As the flow compressibility increases such that $\delta_c > 0.7$, the $E^u(k) \sim k^{-2}$ trend appears (see Fig. 1(b)), due to the formation of large-scale shock waves [1, 2]. The different power law exponents of kinetic spectrum $E^u(k)$ suggests that the large-scale force can strongly influence the energy cascade behavior, and implies the nonuniversality of compressible MHD turbulence state associated with the dimensionless parameter $\delta_c = u_c'/u'$. Additionally, the magnetic spectrum $E^m(k)$ exhibits the $\sim k^{-5/3}$ scaling for all cases studied here, indicating the flow compressibility has little impact on the magnetic energy cascade. As mentioned in the Letter, the magnetic field is mainly dominated by the strong turbulent shear motions at small scales, which can also be observed in Fig. 1(c), in which the compensated spectrum reaches its maximum at moderate wave-numbers.

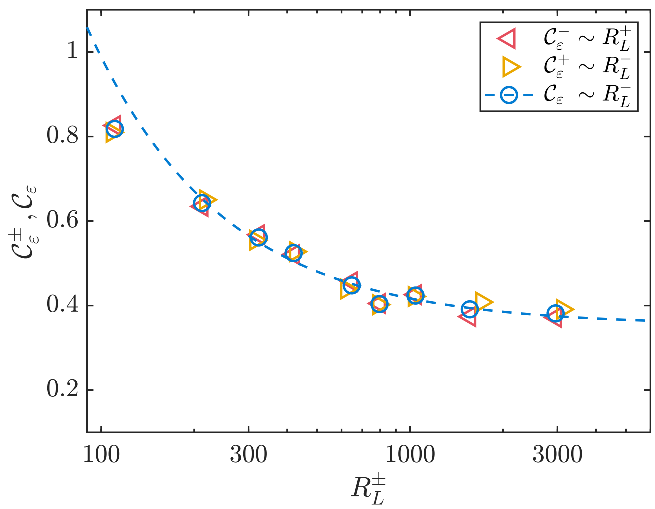

FIG. 2: The normalized dissipation rate versus the generalized large-scale Reynolds number for data from simulation series E. The dashed line indicates the fitting model described in Eq. (8).

THE CHOICE OF $\mathcal{C}_\varepsilon^+$ OR $\mathcal{C}_\varepsilon^-$

In this study, the cross helicity $H_c = \langle \boldsymbol{u} \cdot \boldsymbol{b} \rangle$ and the corresponding spectrum $E_c(\boldsymbol{k}) = \langle \boldsymbol{u}^*(\boldsymbol{k}) \cdot \boldsymbol{b}(\boldsymbol{k}) \rangle$ remain small in all simulation cases. Hence we have

$$\left\langle (\boldsymbol{z}^+)^2 \right\rangle = \left\langle (\boldsymbol{z}^-)^2 \right\rangle , \quad \int_0^\infty k^{-1} E^+(k)\, \mathrm{d}k = \int_0^\infty k^{-1} E^-(k)\, \mathrm{d}k \, . \tag{5}$$

Recall that the key quantities about dissipative anomaly are defined as

$$\mathcal{C}_\varepsilon^\pm = \frac{\varepsilon L_\pm}{(Z_\pm)^2 Z_\mp} , \quad \mathcal{C}_\varepsilon = \frac{1}{2}\left(\mathcal{C}_\varepsilon^+ + \mathcal{C}_\varepsilon^-\right) , \quad R_L^\pm = \frac{\langle \rho \rangle Z_\pm L_\mp}{\langle \mu \rangle} , \tag{6}$$

where $Z_\pm$ and $L_\pm$ denote the rms values and the integral length-scales of the Elsässer variables $\boldsymbol{z}_\pm$. Therefore, in the zero cross helicity cases one should expect that

$$Z_+ = Z_- , \quad L_+ = L_- \quad \Longrightarrow \quad R_L^+ = R_L^- , \quad \mathcal{C}_\varepsilon = \mathcal{C}_\varepsilon^+ = \mathcal{C}_\varepsilon^- , \tag{7}$$

and the following model between $\mathcal{C}_\varepsilon$ and R_L^-

$$\mathcal{C}_\varepsilon = \mathcal{C}_{\varepsilon,\infty} + \frac{\mathcal{D}}{R_L^-} + O\left[(R_L^-)^{-2}\right] \tag{8}$$

is adequate to explore the dissipative anomaly phenomenon.

Fig. 2 depicts the relation between the normalized dissipation rate and the generalized large-scale Reynolds number for DNS series E. Here the relation of $\mathcal{C}_\varepsilon^-$ versus R_L^+ , $\mathcal{C}_\varepsilon^+$ versus R_L^- , and $\mathcal{C}_\varepsilon$ versus R_L^- are all scattered. The fitting curve of $\mathcal{C}_\varepsilon$ versus R_L^- using model (8) is plotted as well. Clearly, the specific choice of $\mathcal{C}_\varepsilon^+(\mathcal{C}_\varepsilon^-)$ and $R_L^-(R_L^+)$ has little impact on the results.

THE CHOICE OF FITTING MODELS

As outlined in the manuscript and suggested by prior studies [3, 4], the following two kinds of models both can be used to quantify the relation between the normalized dissipation rate $\mathcal{C}_\varepsilon$ and generalized Reynolds number R_L^- .

- model-1: Utilizing the first order model

$$\mathcal{C}_\varepsilon = \mathcal{C}_{\varepsilon,\infty} + \frac{\mathcal{D}}{R_L^-} ,$$

and fitting data points with moderate to large Reynolds numbers $(R_L^- \geq 150)$.

TABLE III: The estimate values and standard errors of fitting model coefficients.

Series	model	R2	$\mathcal{C}_{\varepsilon,\infty}$	σ_C	$\mathcal{D}$	σ_D	$\mathcal{F}$	σ_F
A	model-1	0.944	0.506	0.0069	24.16	2.62		
	model-2	0.989	0.500	0.0078	28.89	4.37	-692.3	407.7
B	model-1	0.961	0.370	0.0099	46.57	4.20		
	model-2	0.992	0.362	0.0117	54.54	7.49	-1234.6	711.9
C	model-1	0.981	0.198	0.0161	110.56	6.93		
	model-2	0.994	0.188	0.0238	122.99	15.38	-2660.3	1482.2
D	model-1	0.915	0.410	0.0122	40.31	5.03		
	model-2	0.963	0.399	0.0137	53.85	8.82	-2604.5	880.3
E	model-1	0.964	0.351	0.0117	64.11	5.08		
	model-2	0.987	0.341	0.0139	77.49	9.35	-2726.1	977.7
F	model-1	0.971	0.280	0.0213	117.15	9.08		
	model-2	0.987	0.268	0.0312	134.84	20.08	-4298.8	2080.7

- model-2: Employing the second order model

$$\mathcal{C}_\varepsilon = \mathcal{C}_{\varepsilon,\infty} + \frac{\mathcal{D}}{R_L^-} + \frac{\mathcal{F}}{(R_L^-)^2}\,,$$

  and incorporating all DNS cases, including those with low Reynolds numbers, for fitting.

To compare these models and investigate the influence of the higher-order term $(R_L^-)^{-2}$ on the asymptotic dissipation rate $\mathcal{C}_{\varepsilon,\infty}$, we performed fitting procedures for both models using data from simulation series A-F. (Series P and Q do not involve DNS cases with low Reynolds number, hence are not included in the comparisons).

The estimated model coefficients $\mathcal{C}_{\varepsilon,\infty}\,, \mathcal{D}\,, \mathcal{F}$ are summarized in Table III. The table also includes corresponding standard errors σ_C, σ_D, σ_F, and the coefficient of determination R2 to evaluate the goodness of fit. Remarkably, R2 values consistently surpass 0.91(with most cases exceeding 0.96), while the ratios $\sigma_C/\mathcal{C}_{\varepsilon,\infty}$ and $\sigma_D/\mathcal{D}$ remain small, signifying excellent fits and the ability of both models to describe the $\mathcal{C}_\varepsilon \sim R_L^-$ relationship effectively. Furthermore, the close agreement between estimated values of $\mathcal{C}_{\varepsilon,\infty}$ and $\mathcal{D}$ from both models suggests that considering first-order terms in R_L^- suffices for this study. Notably, the estimated values of $\mathcal{F}$ in the second-order model are consistently negative, in line with findings from incompressible MHD turbulence studies [4].

Figure 3 illustrates the data points alongside the two fitting curves, indicating remarkable alignment when $R_L^- \geq 200$. This convergence indicates that both models yield similar predictions for the asymptotic dissipation rate $\mathcal{C}_{\varepsilon,\infty}$ again.

In summary, above results and discussions underline the capability of both models to elucidate the relationship between the normalized dissipation rate $\mathcal{C}_\varepsilon$ and generalized large-scale Reynolds number R_L^- in compressible MHD turbulence, and the suitability of using first order model for subsequent studies detailed in the manuscript.

---

* wanmp@sustech.edu.cn

[1] J. Wang, Y. Yang, Y. Shi, Z. Xiao, X. T. He, and S. Chen, Phys. Rev. Lett. **110**, 214505 (2013).
[2] Y. Yang, Y. Shi, M. Wan, W. H. Matthaeus, and S. Chen, Physical Review E **93**, 061102 (2016).
[3] M. F. Linkmann, A. Berera, W. D. McComb, and M. E. McKay, Physical Review Letters **114**, 235001 (2015).
[4] M. Linkmann, A. Berera, and E. E. Goldstraw, Physical Review E **95**, 013102 (2017).

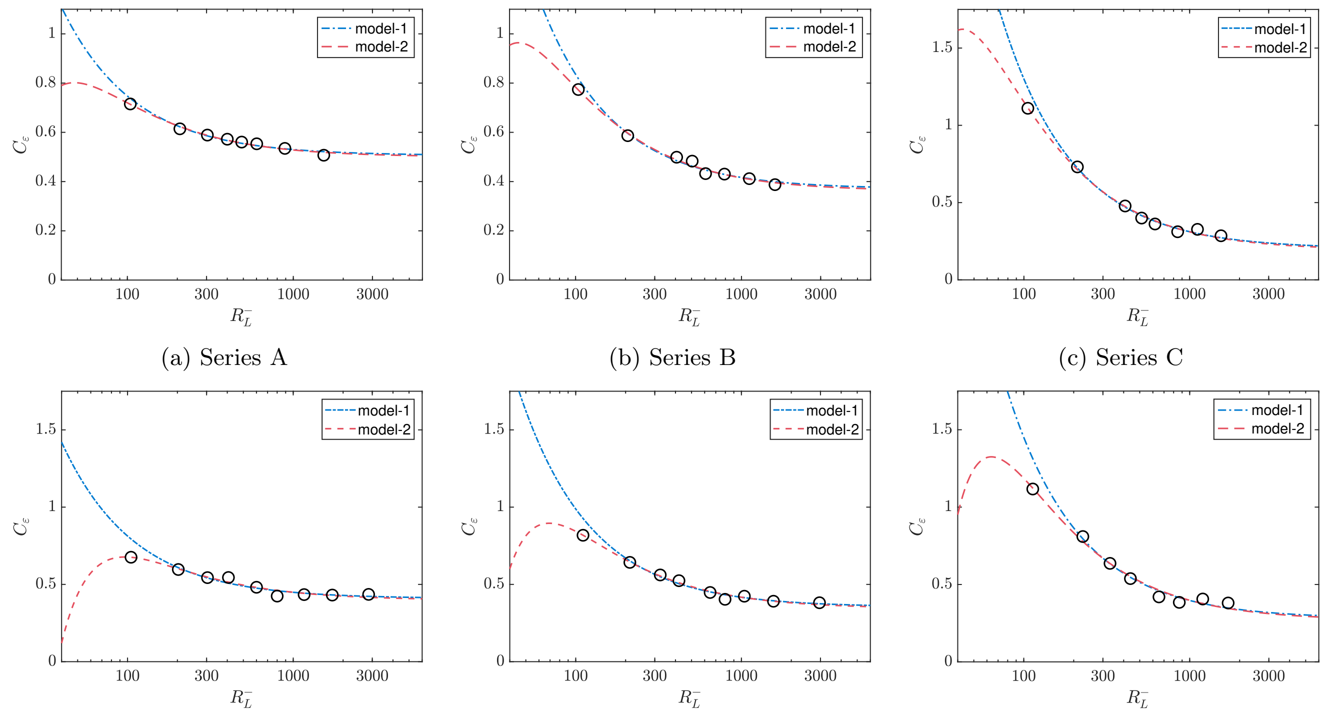

(a) Series A (b) Series B (c) Series C

(d) Series D (e) Series E (f) Series F

FIG. 3: Comparison of two fitting models for DNS series A-F. The circle symbols represent the data points, whereas the lines correspond to the two kinds of fitting curves.